A neutron diffraction study of RMn_2O_5 multiferroics

IOP PUBLISHING JOURNAL OF PHYSICS: CONDENSED MATTER

J. Phys.: Condens. Matter **20** (2008) 434213 (15pp) doi:10.1088/0953-8984/20/43/434213

A neutron diffraction study of RMn_2O_5 multiferroics

P G Radaelli and L C Chapon

ISIS Facility, Rutherford Appleton Laboratory—STFC, OX11 0QX, UK

Received 19 May 2008, in final form 7 July 2008
Published 9 October 2008
Online at stacks.iop.org/JPhysCM/20/434213

Abstract

The magnetic properties of RMn_2O_5 multiferroics as obtained by unpolarized and polarized neutron diffraction experiments are reviewed. We discuss the qualitative features of the magnetic phase diagram in both zero magnetic field and in field and analyze the commensurate magnetic structure and its coupling to an applied electric field. The origin of ferroelectricity is discussed based on calculations of the ferroelectric polarization predicted by different microscopic coupling mechanisms (exchange-striction and cycloidal spin–orbit models). A minimal model containing a small set of parameters is also presented in order to understand the propagation of the magnetic structure along the *c*-direction.

1. Introduction

The recent discovery of a new class of magnetic ferroelectric materials, in which electrical polarization coincides with a magnetic ordering or reordering transition, has generated very significant interest [1–6]. The attractive feature of these materials is not so much the value of the electrical polarization, which is several orders of magnitude smaller than for typical ferroelectrics and even for 'classic' magnetic multiferroics such as $BiFeO_3$, but rather the very large cross-coupling between magnetic and electrical properties, which makes the 'novel' multiferroics enticing paradigms of functional behavior. Although conceptual devices based on novel multiferroics have been discussed [2], none of the materials so far described are directly suitable for applications because the transition temperatures are low. What keeps much of the interest alive, however, is the possibility of discovering an underpinning general principle which could be applied to guide the synthesis of bulk or film materials with better properties. Some basic common facts about these materials have been established with clarity. As for conventional ferroelectrics, electrical polarization emerges as a result of a symmetry-breaking transition from a high-temperature paraelectric phase. Unlike conventional ferroelectrics, however, the primary order parameter for this phase transition is *magnetic* rather than structural: as a result, the overall magneto-structural symmetry is lowered from that of the paramagnetic phase, eventually leading to a polar point group below one of the magnetic transition temperatures. Here, ferroelectricity is induced by some form of magneto-elastic and/or magneto-electronic interaction. On this principle, much work has been published on both group theory [7] and phenomenology [8–10], aimed at establishing the symmetry requirements for the appearance of ferroelectricity, as well as the coupling between different order parameters and the generalized phase diagrams of these materials. Essentially all of these results are independent of the microscopic magneto-electric coupling mechanism. There is in fact no requirement that this mechanism is one and the same for all 'novel' multiferroics—in this case, symmetry would be the single unifying principle. However, establishing this microscopic mechanism in each case is crucial for a quantitative understanding of the phenomenon, and it is an essential guiding principle for engineering new materials. As it happens, most of the 'novel multiferroic' materials so far discovered share much more than a broken magnetic symmetry leading to a polar group: in fact, the presence of a cycloidal component to the magnetic structure in [11, 12, 4, 13–15] suggests a common underlying microscopic mechanism, which is critically dependent on the non-collinearity of the spins. Nagaosa *et al* [16] and Mostovoy [10] explored this concept early on from different angles, and proposed what has now become known as the 'theory of ferroelectricity in cycloidal magnets'. In particular, Nagaosa *et al* have proposed a detailed microscopic model based on the relativistic spin–orbit interaction, which is able to predict qualitatively, and to a certain extent quantitatively, the emergence of ferroelectricity in the presence of a cycloidal (or more generally non-collinear) magnetic structure of appropriate symmetry. It has been known for rather a long time that other mechanisms can potentially induce ferroelectricity even in collinear antiferromagnets.

However, the appeal of a single 'universal' model is strong, and physics based on cycloidal modulations is very often sought as 'the' single explanation for novel multiferroic behavior. The family of compounds with general formula RMn_2O_5 (R = Y, rare-earth, Bi and La) has so far stubbornly resisted being classified with the other compounds in the 'cycloidal multiferroic' family. Three aspects of the RMn_2O_5 phenomenology stand out to suggest that these materials may be in a class of their own: the fact that the direction of the electrical polarization cannot be turned by an applied magnetic field [17], the *commensurate* nature of the magnetic ferroelectric phase (ferroelectricity is all but lost in the low-temperature, incommensurate phase), and the fact that in the ferroelectric phase, moments in the *ab*-plane are almost collinear. The idea that RMn_2O_5 may stand apart from the other multiferroics has recently been challenged by new findings—particularly the evidence for previously unobserved cycloidal components [18, 19]. In this paper, we describe the general phenomenology and present new results on the RMn_2O_5 family multiferroics. We argue that, in spite of the emerging complexity and subtlety of the magnetic structure in these materials, there are still strong reasons to believe that cycloidal physics plays a minor role in RMn_2O_5 (at least for the commensurate phase), and that ferroelectricity emerges due to more conventional exchange-striction effects in the context of a structure with built-in charge ordering.

2. Experimental details

Polycrystalline, single-phase RMn_2O_5 samples were prepared through conventional solid-state reaction in an oxygen environment. Stoichiometric quantities of Tb_4O_7 purity 99.998%, Dy_2O_3 99.99%, Ho_2O_3 99.995%, and MnO_2 99.999% were thoroughly mixed, compressed into pellets and then sintered at 1120 °C for 40 h with intermediate grindings. The samples were finally cooled at 100 °C h^{-1} down to room temperature. Single crystals were prepared using the method described in [19]. Powder neutron diffraction data were collected on the GEM diffractometer at the ISIS facility of the Rutherford Appleton Laboratory (UK). The samples were enclosed in vanadium cans. All the data presented were collected using either a helium cryostat or an Oxford Instrument 10 T cryomagnet. For zero-field experiments, data were always collected on warming, after cooling the sample to base temperature (typically 1.6 K). Experiments performed in magnetic fields were conducted as follows: measurements on the YMn_2O_5 compound were carried out at 1.6 K in a field of 0, 2, 4, 6, 8 T, respectively. For each magnetic field, data were acquired for 2 h. Measurements on the $TbMn_2O_5$ system were carried out in the temperature range 20–34 K, in steps of 1 K, for several values of the magnetic field (0, 1, 3, 5, 7, 9 T). For each measurement, the sample was first zero-field cooled. The magnetic field was then applied and measurements were carried out on warming, setting a counting time of 1 h per temperature. Single-crystal neutron diffraction experiments were recorded at the Institut Laue Langevin (France), using the D10 4-circle diffractometer for unpolarized work and the D3 instrument equipped with CRYOPAD for spherical neutron polarimetry. Details of the experimental procedures can be found in [19] and [20]. Analysis of powder and single-crystal neutron diffraction data were carried out with the software FullProf [21].

3. Crystal structure

The crystal structure of RMn_2O_5 compounds, already described in detail in [22, 19], will be briefly reviewed here. The Mn ions are fully charge ordered, with Mn^{3+} and Mn^{4+} ions occupying sites of different symmetry. Mn^{3+} and Mn^{4+} are respectively coordinated by five oxygens in square pyramid geometry and six oxygens in octahedral geometry, as shown in figure 1. The crystal structure is best described by considering the *ab*-plane configuration and out-of-plane configuration independently. In-plane, octahedra and pyramids are corner-sharing through either the pyramid base or pyramid apex. In addition, adjacent pyramids are connected through their base. In total, three inequivalent exchange paths between magnetic ions exist in the plane (denoted J_3, J_4 and J_5 in figure 1 following the notation of [22]). Along the *c*-axis, octahedral sites are sharing edges, forming linear chains. The Mn^{4+} are located at $z \sim 0.25$ and $(1-z) \sim 0.75$, so that Mn^{3+} ions, positioned at $z = \frac{1}{2}$, form layers in between adjacent Mn^{4+}. R^{3+} ions occupy sites of the same symmetry as Mn^{3+} in the $z = 0$ plane, forming another layer alternating with the Mn^{3+} layer. The ions in the primitive unit cell are labeled following the convention defined in [22, 19], as indicated in figure 1.

4. Magnetic ordering sequence of phase transitions

The RMn_2O_5 structure type has been synthesized with Y, all the lanthanides (excluding Ce) [23–25], Bi [26] and La [23, 27]. Compounds containing lanthanum and all the rare-earths lighter than Nd (included) do not become ferroelectric. The 'typical' features of the magnetic phase diagram of the RMn_2O_5 family are best described based on the temperature-dependent neutron diffraction patterns in figure 2. We can identify three or four regions depending whether the R site is magnetic or not. In the high-temperature paramagnetic phase, only nuclear Bragg peaks are present. On cooling, magnetic Bragg peaks first appear in reciprocal space positions corresponding to an incommensurate propagation vector $q = (\frac{1}{2} - \delta_x, 0, \frac{1}{4} + \delta_z)$. The values of δ_x (resp. δ_z) range from 0.012–0.028 (respectively −0.013–0.027) [28–31, 25, 22, 32–34]. Within this high-temperature incommensurate phase(HT-ICP), the propagation vector changes with temperature, as can clearly be seen from the curved shape of the Bragg peak centroid (this is best seen on peak (0 1 0) $\pm q$ around 7 Å). On further cooling, the values of δ_x and δ_z smoothly approach zero, and the magnetic structure 'locks' into a commensurate phase (CP). The CP is the main ferroelectric phase for most compositions. Below ∼20 K, there is an abrupt transition to a low-temperature incommensurate structure (LT-ICP)—the position of the Bragg peaks continues to change down to the lowest temperatures. Upon entering the LT-ICP,

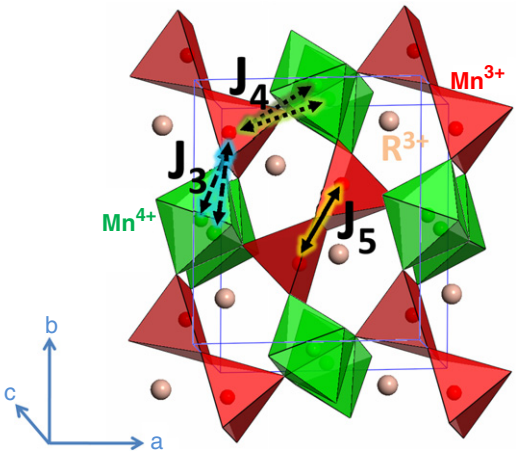

Figure 1. Perspective view of the crystal structure of RMn_2O_5. Mn^{3+}, Mn^{4+} and R^{3+} ions are shown, respectively, as red, green and pink spheres. Polyhedra around Mn^{3+} and Mn^{4+} ions connecting first neighbor oxygens ions are also shown. Magnetic superexchange interactions J_i, $i = 3, 5$ are shown by double sided arrows.

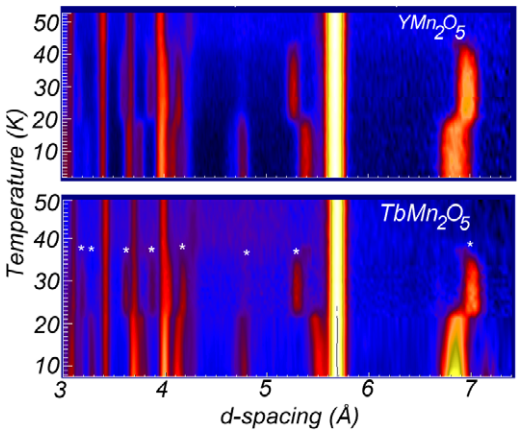

Figure 2. Neutron powder diffraction patterns as a function of temperature for YMn_2O_5 (top) and $TbMn_2O_5$ (bottom) in the magnetically ordered phases. The scattering intensity is color coded with brighter colors representing higher intensities. The intensity of each diagram is normalized to the most intense nuclear reflections in this d-spacing range ((0, 0, 1) peak at 5.8 Å). The positions of magnetic Bragg peaks are indicated by a white asterisk.

the value of the electrical polarization drops to a much smaller value [3], although there seems to be consensus that $P \neq 0$ in some cases (e.g. Y). For Tb, as well as other magnetic rare-earths, the intensity of the magnetic peaks rapidly increased below ∼10 K, indicating that the rare-earth sublattice is becoming magnetically ordered (rare-earth ordered phase, ROP). The ROP is more strongly ferroelectric than the LT-ICP, and displays very large magneto-electric effects [35, 3, 36]. This general magnetic phase diagram, with some subtleties, is shared by RMn_2O_5 with R = Y, Ho, Tb and Er [22, 30, 28, 37, 32, 38], which are the most studied compounds. Excluding the obvious absence of rare-earth ordering for Y and the somewhat different transition temperatures, the most significant differences between these compounds are within the HT-ICS. For Ho and Tb, the two components q_x and q_z of the propagation vector seem to become commensurate at the same temperature, whereas for Er and Y there is a small region where $q_z = \frac{1}{4}$ while q_x remains incommensurate [37]. The connection between this phenomenon and the appearance of 'weak' ferroelectricity have not been thoroughly explored. In fact, hardly anything is known about the HT-ICS other than the propagation vectors, as the small magnetic moments make neutron studies more difficult than in the other phases. Three more compounds were studied in some detail: non-ferroelectric $LaMn_2O_5$ orders with a propagation vector $q = (0, 0, \frac{1}{2})$ [27, 33]; $DyMn_2O_5$ behaves like the other systems with magnetic rare earths above 8.4 K, but displays commensurate ordering with $q = (\frac{1}{2}, 0, 0)$ below this temperature, coexisting with a small fraction of the LT-ICP [39, 33, 34]; the magnetic structure of $BiMn_2O_5$ is commensurate and ferroelectric at all temperatures with a propagation vector $q = (\frac{1}{2}, 0, \frac{1}{2})$ [26, 19].

5. Influence of an applied magnetic field

The strong magneto-electric coupling in these materials can be directly evidenced by measurements of electric properties under a magnetic field. For example in $TbMn_2O_5$, the upward jump in the dielectric constant at the CP to LT-ICP transition is pushed to higher temperatures as a magnetic field is applied [3], suggesting that the LT-ICP phase is stabilized by a magnetic field. This can be directly verified by constructing the H–T phase diagram of the CP–LT-ICP magnetic transition from powder neutron diffraction experiments in a field. Data collected under fields up to 9 T are reported in figure 3. Zero-field data show that the transition from CP to ICP phases is first order, as expected from group theory since the CP and ICP phases are characterized by wavevectors belonging to different symmetry points of the Brillouin zone. The region of co-existence is very narrow and can be estimated to be about 1–2 K. Under application of a magnetic field, the CP–ICP transition temperature is enhanced from ∼25 K in zero-field to more than 27 K at 9 T. The H–T phase diagram, reported in figure 4, has been constructed by fitting the data with two peaks of constrained widths, at positions fixed to the CM and ICP peak positions in zero-field. The transition temperature has been defined as the point of crossover between the intensity of these peaks. The stabilization of the LT-ICP phase under a magnetic field is in perfect agreement with the magnetic and dielectric phase diagrams [3], showing a gradual shift towards high temperatures, on the one hand, of the kink observed in the first derivative of the magnetic susceptibility and, on the other hand, of the upward jump in the dielectric constant. The CP to LT-ICP transition is also smoothed out by the magnetic field. Under a field, the temperature range of the co-existence of CP/LT-ICP phases is extended, while the propagation vectors of both phases do not seem to be altered. Overall, the magnetic behavior obtained by powder neutron diffraction data shows that the low-temperature ICP phase is stabilized by application of an external field. This result is opposite to that recently published on the analogue compound $HoMn_2O_5$ [40], showing that the boundary between CP and ICP phases is shifted to a lower

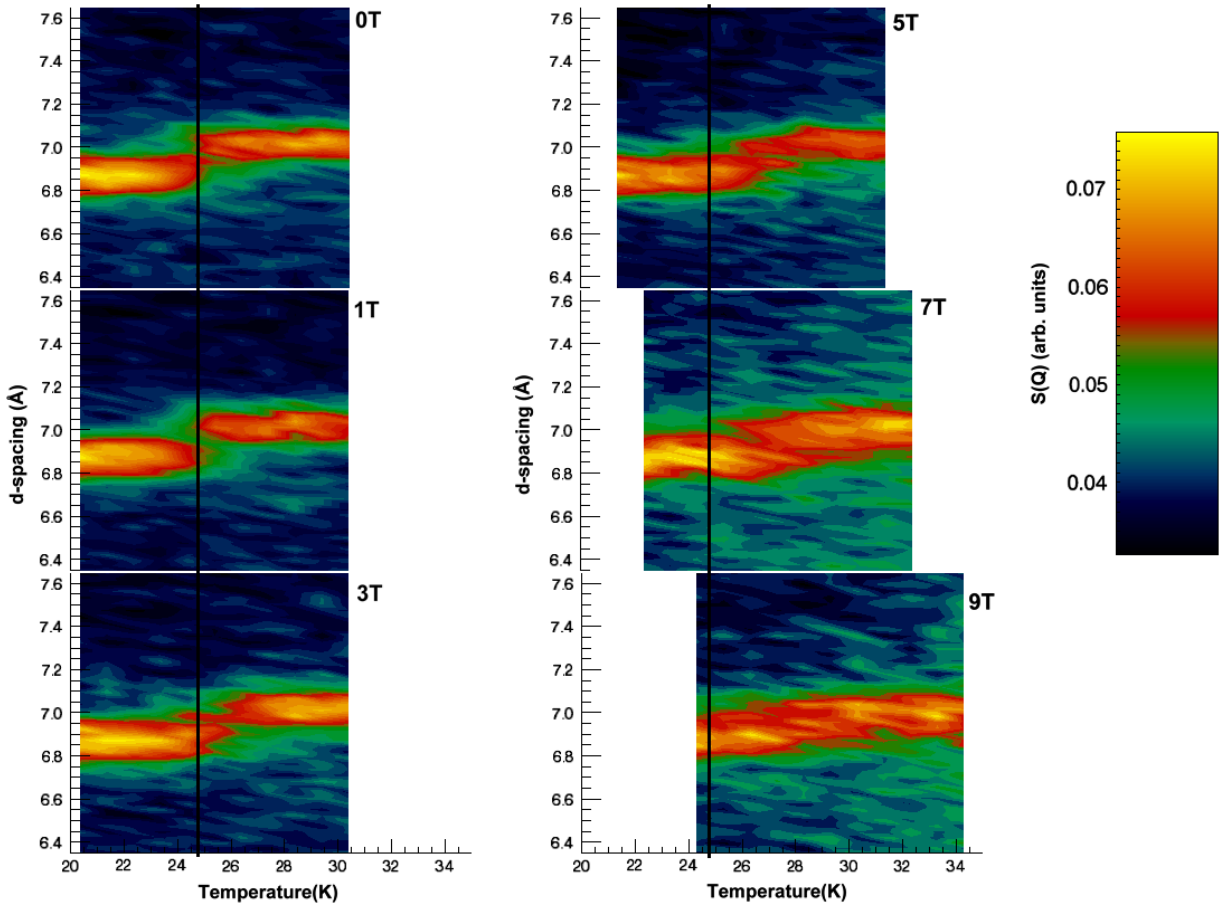

Figure 3. Dependence of the (100)-k magnetic reflection with temperature and applied magnetic field for $TbMn_2O_5$. The scattering intensity is color coded and displayed as a function of d-spacing and temperature for several values of the magnetic field. The color scale is shown on the right. A vertical line is displayed to mark the zero-field ICP–CP transition temperature.

temperature under application of a magnetic field along the b-axis. In both cases (Tb, Ho), neutron data correlate directly to the electric properties under a magnetic field, confirming fundamentally different behaviors. Nevertheless, it should be noted that experiments reported for the Ho system [40] and here have been conducted in different conditions. Work on $HoMn_2O_5$ was performed on a single crystal and only a magnetic field parallel to the b-axis was found to induce the ICP–CP transition. Work on powders is more qualitative due to the random orientation of crystallites with respect to the magnetic field direction. However, the general trend should not be affected by powder averaging, since magnetic fields along a and c proved to only slightly affect the magnetic state of $TbMn_2O_5$. On the other hand, for $HoMn_2O_5$, the induced CP state at high field is observed only in field cooled experiments, whereas zero-field cooled process leave the low-temperature ICP phase unchanged up to 13 T. This indicates a large hysteresis (greater than 2 T), as pointed out by Kimura *et al*, due to the first order nature of the transition. However, this does not explain the opposite variation of the CP–ICP temperature boundary in the H–T phase diagram, and it is more likely that the discrepancy is a direct consequence of different single-ion anisotropies of the rare-earth ion (R) and its related effects on the Mn(d)–R(f) coupling. Another perspective in the comparison

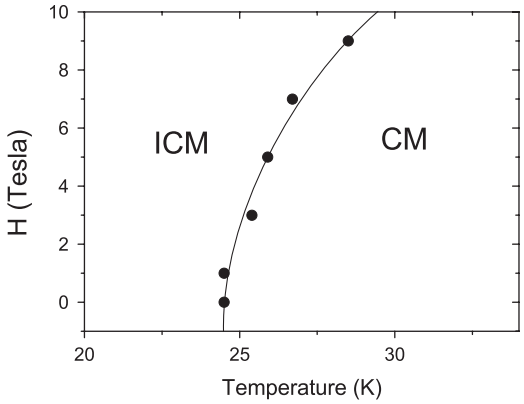

Figure 4. H–T phase diagram of the commensurate (CM) to incommensurate (CM) phase transition in $TbMn_2O_5$. The points have been calculated by a fitting procedure (see text for details). The solid line is a guide to the eye.

between Ho and Tb systems is given by their magnetic behavior at low temperatures. Tb ions order magnetically below 10 K with the same propagation vector describing ordering of the Mn sublattice, i.e. $\mathbf{k} \sim (0.48, 0, 0.31)$ [32]. Under a moderately low magnetic field (2.5 T), Tb orders

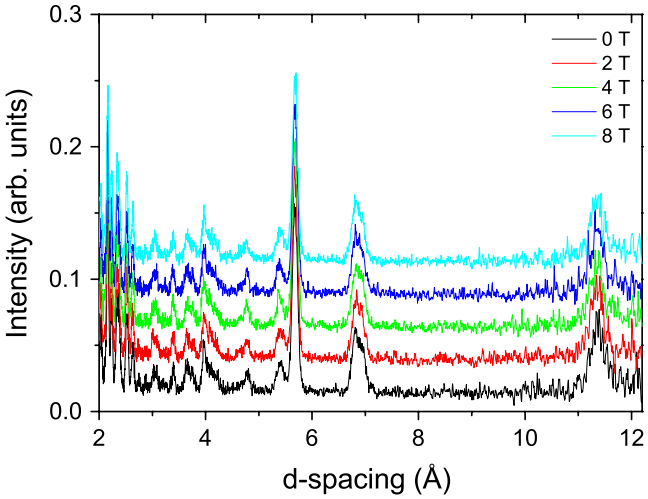

Figure 5. Time-of-flight diffraction patterns of YMn_2O_5 at 1.6 K under magnetic fields between 0 and 8 T.

ferromagnetically, i.e. at $\mathbf{k} = 0$, without any noticeable change in the magnetic structure of the Mn ions. This behavior is in sharp contrast with the results on Ho [40], where it appears that the magnetic ordering of the Mn and Ho sublattices arises at a single point in reciprocal space (CP or ICP) irrespective of the value of the magnetic field, suggesting a stronger d–f coupling. Moreover, the ferroelectric properties of $TbMn_2O_5$ can be understood by the simple superimposition of several order parameters associated with the Mn and Tb sublattices [3], implying the absence of coupling terms between them. We suggested that magnetic ordering of the Mn ions in $TbMn_2O_5$ is unaffected by the field-induced FM ordering of Tb based on indirect evidence, since the subtraction of the 15 K zero-field data from the 1.5 K, 2.5 T data, left an essentially perfect ferromagnetic pattern. This behavior can be verified by in-field neutron diffraction experiments on the analog YMn_2O_5. This compound shows exactly the same sequence of CP–ICP transitions on cooling, but containing a non-magnetic R site. Figure 5 presents powder neutron diffraction patterns obtained in zero field and in fields up to 8 T. The positions of the magnetic Bragg peaks remain unchanged under magnetic field, indicating that the propagation vector of the Mn magnetic structure does not vary. Also the magnetic peak intensities do not change within the error bars, confirming that the orientation of the magnetic moments remains unchanged. These results are in agreement with magnetization measurements in very high magnetic field, showing an extremely stable AFM structure at low temperature and an absence of metamagnetic transitions for the Mn sublattice up to 40 T. Taken together with previous experiments on $TbMn_2O_5$, this tends to favor a picture in which the Mn and Tb magnetic sublattices are fully decoupled, since the metamagnetic transition of Tb does not influence the magnetic ordering of Mn. The situation for the Ho compound is therefore significantly different.

6. Magnetic structures

The magnetic structures of RMn_2O_5-type compounds have been studied since the 1970s [41, 42], and later in the 1980s [43] when the interest in them was mainly for reasons of their unusual complexity. A continuous improvement of experimental and analytical techniques has led to a refinement in their understanding, which in the case of the incommensurate phases has not reached completion yet (see section 11). The magnetic structure is best understood in terms of magnetic a–b planes that are coupled along the c-axis. All the ferroelectric phases share closely related in-plane structures, characterized by the doubling (for the CP) or near-doubling (for the ICP) of the magnetic a-axis, while for non-ferroelectric $LaMn_2O_5$ (propagation vector $(0, 0, \frac{1}{2})$ [27] the a-axis is not doubled. In particular, for all the commensurate, strongly ferroelectric phases, the in-plane magnetic structures are essentially identical. This suggests that the in-plane arrangement of the spins plays a key role in inducing ferroelectricity. On the contrary, the stacking of magnetic layers along the c-axis varies considerably from one compound to the next: $BiMn_2O_5$ [26, 19] and $DyMn_2O_5$ [22, 33, 39] have a simple $\cdots + - + - \cdots$ and $\cdots + + + + \cdots$ staking, respectively, whereas for the other phases the stacking is either exactly (CP) or approximately (ICP) $\cdots + + - - + + - - \cdots$.

As a typical example, the CP structure of YMn_2O_5 is shown in figure 6—the figure also illustrates the symmetry-inequivalent magnetic interactions and their coupling constants. In understanding how this structure is established, the following factors need to be taken into account:

(i) *Exchange interactions.* Although no detailed calculation has been presented so far, the in-plane interactions are likely to be uniformly antiferromagnetic. The interactions along the a direction are particularly strong, so that the presence of AFM zig-zag chains running along this direction is a common motif for all phases. For the LT-ICP, all magnetic structure determinations so far presented agree in evidencing a long-wavelength modulation of this motif, although the details of this modulation differ.

(ii) *Frustration.* The simultaneous presence of antiferromagnetic interactions and *fivefold* exchange rings in the crystal structure immediately leads to a frustrated situation, where not all these interactions can be satisfied simultaneously. In the CP and ICP phases, this situation is relieved in different ways, possibly involving relaxation of the lattice and electronic structures and phasing of the zig-zag chains. Some of the resulting magnetic structures are acentric and capable of supporting ferroelectricity through magneto-elastic or magneto-electronic coupling. Although the matter is still controversial, we believe that this relaxation provides the primary explanation for the ferroelectric phase diagram of these materials.

(iii) *Anisotropy.* It is well known that Mn^{3+} ions with low-lying t_{2g} orbitals tend to be magnetically anisotropic. For octahedral coordination (e.g. in $LaMnO_3$, [44]), the anisotropy is related to the Jahn–Teller distortion—the spin direction *parallel* to the unfilled d_{z^2} orbitals is favored. In $TbMnO_3$ and other cycloidal multiferroics,

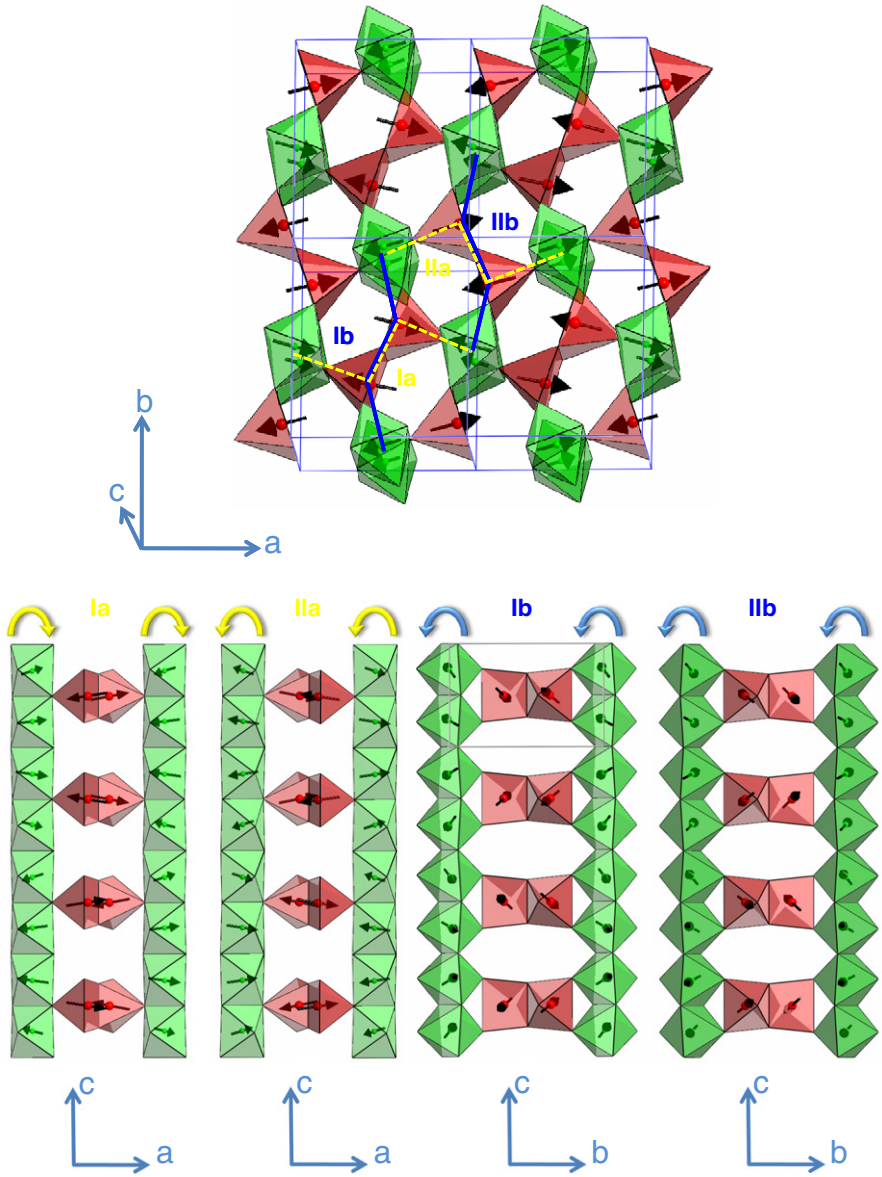

Figure 6. Representation of the commensurate magnetic structure at 25 K. The model is derived from analysis of single-crystal neutron diffraction data. Magnetic ions are represented with the same color scheme defined in reference [19]. Magnetic moments are represented by black arrows. Top panel: magnetic configuration in the *ab*-plane (2×2 unit cells) showing the presence of nearly antiferromagnetic zig-zag chains (see text for details). Several Mn^{4+}–Mn^{3+}–Mn^{3+}–Mn^{4+} fragments in the structure are labeled with roman numerals (Ia and IIa along the *a*-axis and Ib, IIb along the *b*-axis). Bottom panel: magnetic structure projected in the *ac*- and *bc*-planes. Configurations within each fragment (Ia, IIa, Ib, IIb) are shown for four unit cells along the *c*-direction. The curled arrows at the top of each magnetic chain represent the direction of rotation of the cycloidal modulation. For clarity, the size of the magnetic moment has been doubled for representing modulations in the *bc*-plane (Ib, IIb).

the interplay between anisotropy (favoring collinear magnetic structures) and competing interactions (favoring cycloidal magnetic structures) is thought to be primarily responsible for the magnetic phase diagram—the former and latter arrangements are prevalent at high and low temperature, respectively. In RMn_2O_5, Mn^{3+} has a pyramidal coordination, where the effect of the crystal field is very similar to the Jahn–Teller octahedral case. Consequently, the RMn_2O_5 compounds also display significant anisotropy: in the CP, spins in each of the zig-zag chains are parallel to each other and to the axes of the pyramids. The axes of the pyramids are rotated by about $\pm 15°$ away from the *a* axis, explaining why the *a*-axis component of the spins, S_x, is much larger than the other two and also why the CP magnetic structure is slightly non-collinear.

(iv) *c-axis stacking*. As shown in figures 1 and 6, stacking along the *c*-axis is mediated by crystallographic chains of edge-sharing $Mn^{4+}O_6$ octahedra. To avoid confusion with the zig-zag chains running along the *a*-axis, we will refer to these structures as '*c*-axis ribbons'. Here, there are two relevant magnetic interactions: through

the Mn^{3+} layers (J_2) and through the R layers (J_1) as shown in figure 7. The Mn^{3+}–Mn^{4+} superexchange interactions through the common oxygen atoms appear to be the strongest contributors to J_2 which is therefore always ferromagnetic regardless of the sign of the in-plane interactions J_3 and J_4 (figure 1). Consequently, in all phases, the spins in Mn^{3+} ions adjacent through a Mn^{4+} layer are *always* close to being parallel. We take advantage of this to simplify the description of the c-axis stacking, so that a single sign $+$ or $-$ actually represents two quasi-parallel Mn^{3+} sites. The situation with the coupling J_1 through the R layer is significantly more complex, explaining the diversity of the c-axis components q_z of the magnetic propagation vectors. In the case of $BiMn_2O_5$ and $DyMn_2O_5$, J_1 is AFM or FM, respectively, and strong enough to enforce antiparallel ($\cdots + - + - \cdots$, propagation vector $q = (\frac{1}{2}, 0, \frac{1}{2})$) or parallel ($\cdots + + + + \cdots$, propagation vector $q = (\frac{1}{2}, 0, 0)$) stacking, respectively. In all the other cases, J_1 must be small, since both quasi-parallel and quasi-antiparallel stacking are found within the same magnetic structures.

(v) *Next-nearest-neighbor (NNN) and antisymmetric interactions*. At present, it is not known what determines the c-axis stacking, and the corresponding q_z in materials other than $DyMn_2O_5$ and $BiMn_2O_5$. Two main effects are thought to be responsible for complex stacking and incommensurability in magnetic materials: competition between nearest- and next-nearest-neighbor interaction and the antisymmetric Dzyaloshinskii–Moriya (DM) coupling. The former is the accepted mechanism for explaining the cycloidal phases in $TbMnO_3$ and other cycloidal multiferroics. An analogous model that can be applied to RMn_2O_5 will be discussed in section 8. It has recently been shown [18, 19] that in the CP of several RMn_2O_5 compounds, including $BiMn_2O_5$, a small c-axis component S_z of the spins is present, and that in the first approximation this is out of phase with respect to the other two components, giving rise to very flat cycloids running along the c-axis. It is interesting to remark that this component is present *regardless* of the propagation vector, although it is smaller in the case of $BiMn_2O_5$. For $BiMn_2O_5$, there is a very simple explanation for the appearance of a c-axis component of this kind, due to the antisymmetric DM interaction (see section 9 below). It is tempting to extend this explanation to the other phases as well, and conclude that CP flat cycloids are of DM origin. We remark, however, that no detailed models or calculations have been presented so far.

Leaving the small S_z component aside, the general features of the in-plane magnetic structures of RMn_2O_5 in the CP regime can be rationalized very well based on points (i)–(iii) above. From figures 1 and 6, it can clearly be seen that in the absence of structural distortions, there is an exact cancelation of all energy terms containing J_3, since pairs of ions related by inversion symmetry carry magnetic configurations of opposite sign. This situation gives rise to the so-called magnetic Jahn–Teller effect, due to the analogy

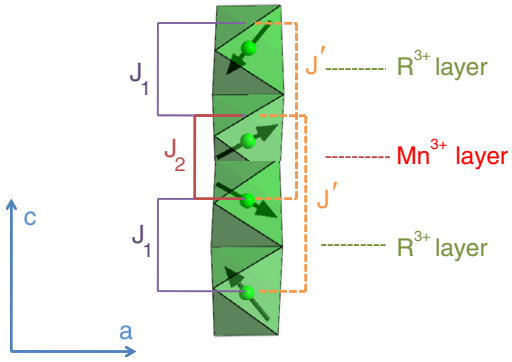

Figure 7. Labeling scheme and relevant interactions for the linear-chain model discussed in this section. One of the possible spin ordering modes is shown.

with the well-known structural effect. Here, the system can always gain energy from distortion of the crystal or electronic structure that makes the J_3 slightly inequivalent, since the energy gain is linear and the energy cost is typically quadratic in the distortion. We have previously argued [32, 38] that this is the primary mechanism leading to the appearance of ferroelectricity in RMn_2O_5 (see next section).

7. Origin of ferroelectricity

Two main models have been proposed to explain the appearance of ferroelectricity in the CP of RMn_2O_5; here, we will refer to these models as the symmetric exchange-striction model and the cycloidal model, respectively. These two models are at present very difficult to disentangle based on the facts known to us with confidence. In particular, the point-group symmetry of the CP, which has been solved with great accuracy, is still very high ($m2m$; see [7]), so the ferroelectric polarization *must* lie along the b-axis, regardless of the mechanism.

The exchange-striction model relies on the magnetic Jahn–Teller effect as its main ingredient: here, electrical polarization would arise from a combination of atomic displacements and electronic rearrangements, removing the exact exchange degeneracy. The main features of the exchange-striction model are:

- The most important element controlling ferroelectricity is the in-plane components of the magnetic structure. Non-collinearity is not an essential ingredient, as it has been shown that the same effect can be obtained in a collinear acentric structure. The stacking along the c-axis is immaterial and so is the small c-axis component, provided that all the layers have the same polarization.
- Quantitatively, the electrical polarization is proportional to the *scalar* product of spins related by J_3 in different zig-zag chains. Therefore, the relative phasing of the two chains is directly related to the magnitude of the polarization [38]. In the CP, this relative phase is uniform, so that each J_3 pair contributes equally to the ferroelectricity. However, there is no reason for this to be so in the LT-ICP—in fact for all models of the ICP

so far proposed the *scalar* product varies in both sign and magnitude along the propagation direction. This provides an immediate explanation for the sudden loss of ferroelectricity in the LT-ICP (see below).

- As mentioned before, in the CP the electrical polarization is *always* directed along the *b*-axis by symmetry. With all probability, there is a similar requirement for the incommensurate phases, so that whatever residual polarization remains in the LT-ICP should also be directed along the *b*-axis, in agreement with all the experiments. Very recent electronic structure calculations [45, 46] have provided evidence that ferroelectricity can be explained without invoking spin–orbit coupling.

The cycloidal model relies on the same spin–orbit-driven *inverse* Dzyaloshinskii–Moriya effect that has been used to explain the physics of $TbMnO_3$ and other cycloidal magnets: here, electrical polarization would arise again from a combination of atomic displacements and electronic rearrangements, but this time what is minimized is the *antisymmetric* interaction between non-collinear spins. The general expression for the polarization thus generated is $\mathbf{P} \propto \mathbf{e}_{12} \times (\mathbf{S}_1 \times \mathbf{S}_2)$, where $\mathbf{S}_1$ and $\mathbf{S}_2$ are spins on adjacent sites along the *c*-axis and $\mathbf{e}_{12}$ is a unit vector connecting them (see, for example, [5]).

The main features of the cycloidal model are:

- It provides a unified, 'universal' explanation for all novel multiferroics. This is perhaps the most important reason for its popularity.
- Non-collinearity in the context of a cycloidal structure is an essential ingredient of the model.
- Locally, the polarization direction is defined by the cross product of two vectors, **u**, which is perpendicular to the plane of rotation of the spins, and $\mathbf{q}'$, defined as the projection of the propagation vector **q** along the direction of the bonds contributing to antisymmetric exchange. $\mathbf{q}'$ may be difficult to define in general, because several bonds could provide independent contributions, but in the case of the CP, $\mathbf{q}'$ is directed along the *c*-axis. The contribution to the electrical polarization of different ribbons may cancel in some directions. For example, in the CP, the plane of rotation of the flattened cycloids is defined by the *c*-axis and by the anisotropy direction, which is rotated 15° away from the *a*-axis. However, the large P_x components cancel out between the two ribbons in the unit cell, whereas the smaller P_y components add, yielding an overall polarization along the *b*-axis. Once again, this is entirely due to symmetry.
- Preliminary investigations [47] indicate that the LT-ICP has lower symmetry than the CP, but the polarization is still required to lie along the *b* direction. A precise LT-ICP solution of the magnetic structure may be able to discriminate conclusively between the two mechanisms.

Most of the considerations so far are qualitative. However, it is possible to make a quantitative assessment of the likely contributions of both exchange-striction and cycloidal mechanisms, once the magnetic structures are known in detail. What can never be known from the magnetic structure alone are the coupling constants for symmetric and antisymmetric exchange, although it is reasonable to assume that the antisymmetric coupling should be weaker, since it relies on the intrinsically weak spin–orbit mechanism. In both cases, the electrical polarization **P** is obtained by multiplying the appropriate coupling constant times a polar vector (**E** or **S** below), which is entirely defined by the magnetic structure and has the dimension of μ_B^2. For the calculation of these polar vectors, only the spins within one unit cell need to be taken into account, once the propagation vector is known. Therefore, the same formalism can be applied to the CP and to all the ICPs. For the calculations presented in this section, we employ the following convention: the three components of the magnetic moment of a given site s, V_i^s $(i = x, y, z)$ in unit cell R_l, are:

$$V_i^s(R_l) = M_i^s \cos(q R_l + \phi_i^s). \tag{1}$$

M_is and ϕ_is can be calculated from the Fourier coefficients given in [19]. We note that the propagation vector q and phase ϕ are given here in radians and not in fractional units of 2π [19]. The same labels as in [22, 19] are employed for magnetic ions in the unit cell.

The exchange-striction polar vector E_y is always directed along the *b*-axis. If q_x is incommensurate, E_y is calculated as

$$\begin{aligned} E_y = \tfrac{1}{2} \sum_{i=1,3} & M_i^{b2} M_i^{a1} \cos(\phi_i^{b2} - \phi_i^{a1}) \\ & + M_i^{b1} M_i^{a1} \cos(\phi_i^{b1} - \phi_i^{a1}) \\ & - M_i^{b2} M_i^{a4} \cos(\phi_i^{b2} - \phi_i^{a4} + q_x) \\ & - M_i^{b1} M_i^{a4} \cos(\phi_i^{b1} - \phi_i^{a4} + q_x) \\ & + M_i^{b3} M_i^{a2} \cos(\phi_i^{b3} - \phi_i^{a2}) + M_i^{b4} M_i^{a2} \cos(\phi_i^{b4} - \phi_i^{a2}) \\ & - M_i^{b3} M_i^{a3} \cos(\phi_i^{b3} - \phi_i^{a3}) - M_i^{b4} M_i^{a3} \cos(\phi_i^{b4} - \phi_i^{a3}). \end{aligned} \tag{2}$$

If $q_x = \pi$, there is an additional 'umklapp' term, so that

$$\begin{aligned} E_y = \sum_{i=1,3} & M_i^{b2} M_i^{a1} \cos\phi_i^{b2} \cos\phi_i^{a1} \\ & + M_i^{b1} M_i^{a1} \cos\phi_i^{b1} \cos\phi_i^{a1} \\ & - M_i^{b2} M_i^{a4} \cos\phi_i^{b2} \cos(\phi_i^{a4} + q_x) \\ & - M_i^{b1} M_i^{a4} \cos\phi_i^{b1} \cos(\phi_i^{a4} + q_x) \\ & + M_i^{b3} M_i^{a2} \cos\phi_i^{b3} \cos\phi_i^{a2} + M_i^{b4} M_i^{a2} \cos\phi_i^{b4} \cos\phi_i^{a2} \\ & - M_i^{b3} M_i^{a3} \cos\phi_i^{b3} \cos\phi_i^{a3} - M_i^{b4} M_i^{a3} \cos\phi_i^{b4} \cos\phi_i^{a3}. \end{aligned} \tag{3}$$

There are two separate components of the spin–orbit polar vector, referring to the cross product of spins across the Mn layer (S^1) or across the RE layer (S^2). The same formula serves to calculate both x and y components. For $q_z \neq \pi$ we obtain:

$$\begin{aligned} S_i^1 = \tfrac{1}{2}\big[& M_i^{b1} M_z^{b_2} \cos(\phi_i^{b1} - \phi_z^{b2}) - M_z^{b1} M_i^{b2} \cos(\phi_z^{b1} - \phi_i^{b2}) \\ & + M_i^{b3} M_z^{b4} \cos(\phi_i^{b3} - \phi_z^{b4}) - M_z^{b3} M_i^{b4} \cos(\phi_z^{b3} - \phi_i^{b4}) \big] \\ S_i^2 = \tfrac{1}{2}\big[& M_i^{b2} M_z^{b_1} \cos(\phi_i^{b2} - \phi_z^{b1} - q_z) \\ & - M_z^{b2} M_i^{b1} \cos(\phi_z^{b2} - \phi_i^{b1} - q_z) \\ & + M_i^{b4} M_z^{b3} \cos(\phi_i^{b4} - \phi_z^{b3} - q_z) \\ & - M_z^{b4} M_i^{b3} \cos(\phi_z^{b4} - \phi_i^{b3} - q_z) \big] \end{aligned} \tag{4}$$

whereas for the umklapp case $q_z = \pi$ of $BiMn_2O_5$ we obtain:

$$S_i^1 = M_i^{b1} M_z^{b_2} \cos\phi_i^{b1} \cos\phi_z^{b2} - M_z^{b1} M_i^{b2} \cos\phi_z^{b1} \cos\phi_i^{b2} + M_i^{b3} M_z^{b4} \cos\phi_i^{b3} \cos\phi_z^{b4} - M_z^{b3} M_i^{b4} \cos\phi_z^{b3} \cos\phi_i^{b2}$$
$$S_i^2 = S_i^1. \tag{5}$$

The total polarization is given by

$$P_x = c_1^{so} S_x^1 + c_2^{so} S_x^2$$
$$P_y = c^{es} E_y + c_1^{so} S_y^1 + c_2^{so} S_y^2 \tag{6}$$

where c_1^{so}, c_2^{so} and c^{es} are magneto-elastic coupling constants and can have either sign.

Calculated data for the different polar vector components based on published magnetic structures are reported in table 1. The following observations can be made:

(i) In the strongly ferroelectric CPs, the exchange-striction polar vector E_y is always much larger than the cycloidal polar vectors—typically by a factor of 50–100. This is in itself a strong indication that exchange striction should be the dominant mechanism if one considers the fact that the exchange-striction coupling constants are also expected to be larger.

(ii) We have reported for comparison the polar vector components for the most recently published refinement of the YMn_2O_5 ICP by Kim *et al* [48]. This structure contains cycloids in the *a–b* plane as well, which could in principle contribute to the ferroelectricity through the spin–orbit coupling mechanism. We observe, however, that the strong decrease of E_y is in accord with the drop in the electrical polarization, as observed experimentally. The decrease in E_y is due to the fact that the zig-zag chains are now out-of-phase rather than in-phase, as we remarked for the ICP structure we previously obtained from powder data [38]. On the contrary, the trend on the cycloidal polar vector components—in particular the prediction of a significant polarization along the *a*-axis—is inconsistent with the experiments.

(iii) The large value of E_y calculated for $BiMn_2O_5$ is in agreement with the experimentally observed large polarization. However, our magnetic structure would be consistent with a spin–orbit polarization directed along the *x*-axis, at odds with the experiments. Nevertheless, a more precise determination of the s_z components, which are very small for $BiMn_2O_5$, would be required to be able to employ this argument with confidence to validate the exchange-striction model.

Table 1. Magnetic polar vector components relevant for the exchange-striction mechanism (E_y) and the spin–orbit mechanism (S_x^1, S_y^1, S_x^2 and S_y^2), calculated from equations (2)–(5) for different RMn_2O_5 compounds. We employed our data for the CPs, whereas for the ICP of YMn_2O_5 we used the recent data of Kim *et al* [48]. All values are in μ_B^2. The different signs of E_y are not significant, since they are due to the inversion-domain variant chosen for the refinement.

Compound	**q**	E_y	S_x^1	S_y^1	S_x^2	S_y^2
YMn_2O_5 CP [19]	$(\frac{1}{2}, 0, \frac{1}{4})$	22.6	−0.01	−0.16	−0.04	−0.39
YMn_2O_5 ICP [48]	(0.48, 0, 0.29)	6.8	−5.84	1.34	−4.88	−0.49
$HoMn_2O_5$ CP [19]	$(\frac{1}{2}, 0, \frac{1}{4})$	27.4	−0.10	−0.23	−0.21	−0.46
$BiMn_2O_5$ CP [19]	$(\frac{1}{2}, 0, \frac{1}{2})$	−45.4	−1.38	0.08	−1.38	0.08

8. A simple model for the propagation along the *c*-axis

The magnetic phase diagram of the RMn_2O_5 compounds has been studied phenomenologically in great detail by Harris and co-workers [49, 50]. In this section, we propose a more modest approach, based on the well-known linear-chain model, which, however, contains the minimal ingredients—competition between nearest-neighbor (NN) and next-nearest-neighbor (NNN) interactions, widely thought to be responsible for the observed cycloidal structures in $TbMnO_3$ and related compounds. The purpose of this discussion is to ascertain whether these ingredients are sufficient to explain the general tendency of RMn_2O_5 to develop an out-of-phase s_z component for a variety of propagation vectors.

The spins and interactions to be considered, as shown in figure 7, are:

$$\mathbf{s}_3' = \hat{\mathbf{i}}\, s_x \cos(\beta R_z - \alpha/2 + \beta) + \hat{\mathbf{k}}\, s_z \sin(\beta R_z - \alpha/2 + \beta)$$
$$\mathbf{s}_1 = \hat{\mathbf{i}}\, s_x \cos(\beta R_z + \alpha/2) + \hat{\mathbf{k}}\, s_z \sin(\beta R_z + \alpha/2)$$
$$\mathbf{s}_2 = \hat{\mathbf{i}}\, s_x \cos(\beta R_z - \alpha/2) + \hat{\mathbf{k}}\, s_z \sin(\beta R_z - \alpha/2)$$
$$\mathbf{s}_3 = \hat{\mathbf{i}}\, s_x \cos(\beta R_z + \alpha/2 - \beta) + \hat{\mathbf{k}}\, s_z \sin(\beta R_z + \alpha/2 - \beta) \tag{7}$$

where $\hat{\mathbf{i}}$ and $\hat{\mathbf{k}}$ are unit vectors in the xy-plane and z directions, respectively, R_z is the unit cell index, β is the propagation vector component along z and $\alpha/2$ is the phase of the spins, the latter two being expressed in radians, so that they relate to the tabulated values as $\alpha = 4\pi\delta$ and $\beta = 2\pi q_z$ [19]. Here, s_x and s_z refer to a generic in-plane component and to an out-of-plane component, respectively.

We can construct an idealized two-dimensional model, coupled through NN interactions (J_1 and J_2, which are different) and NNN interactions (J'). The total energy per unit cell is

$$E = \frac{1}{N} \sum_{R_z} J_2\, \mathbf{s}_1 \cdot \mathbf{s}_2 + \frac{1}{2} J_1 \left(\mathbf{s}_1 \cdot \mathbf{s}_3' + \mathbf{s}_2 \cdot \mathbf{s}_3\right) + \tfrac{1}{2} J' \left(\mathbf{s}_1 \cdot \mathbf{s}_3 + \mathbf{s}_2 \cdot \mathbf{s}_3'\right) + \Gamma\, s_z^2 \left(\sin^2(\beta R_z + \alpha/2) + \sin^2(\beta R_z - \alpha/2)\right). \tag{8}$$

The last term containing Γ represents the contribution of the anisotropy. By replacing the expressions of the spins from equation (7) and decomposing the energy into the normal and

umklapp terms $E = E_N + E_U$ we obtain:

$$E_N = \frac{s_x^2 + s_z^2}{2}(J_2 \cos\alpha + J_1 \cos(\alpha - \beta) + J' \cos\beta) + \Gamma s_z^2 \tag{9}$$

$$E_U = \frac{s_x^2 - s_z^2}{2N} \sum_{R_z} \cos(2\beta R_z)\big(J_2 + J_1 \cos\beta + J' \cos(\alpha - \beta)\big) - \Gamma \frac{s_z^2}{N} \sum_{R_z} \cos(2\beta R_z) \cos\alpha. \tag{10}$$

One can easily see from equation (9) that the umklapp term is non-zero only for $\beta = 0$ and π (doubling of the unit cell along the z-axis).

Let us first consider the general case in which the umklapp term is zero. We note that we can ignore the anisotropy when we minimize the energy as a function of the two angles α and β, since the anisotropy term does not contain the angles. By defining $R = J'/J_2$ and $T = J_1/J_2$ and setting the first derivatives to zero we obtain the two solutions:

$$\sin\alpha = -R \sin\beta \qquad \text{with } \sin\beta = 0$$
$$\text{or } \cos\beta = \frac{T}{2}\left(\frac{1}{R^2} - 1\right) - \frac{1}{2T}. \tag{11}$$

The first solution *always* gives rise to umklapp since $\beta = 0$ or π, so it should always be discarded. We can always set $\beta > 0$, whereas α is set in the appropriate quadrant to satisfy equation (11). Once this is done, one should obtain the values of s_x and s_z under the constraint that the total spin at any site cannot exceed the full ionic value ($3/2\mu_B$ for Mn^{4+}). For an elliptical cycloid of this type, the maximum spin value is $\max(s_x, s_z) = s_x$, i.e. the long semi-axis of the ellipse. Therefore, regardless of the specific values of α and β, the minimum energy is always attained for either $s_z = s_x$ (small anisotropy, circular cycloid) or $s_z = 0$ (large anisotropy, collinear spin density wave).

The two situations riving rise to umklapp are $\beta = 0$ and π. We note that in this simple model we cannot obtain the $\beta = \pi/2$ lock-in situation that characterizes the ferroelectric phase. In order for this to occur, one would need a quartic term in the free energy—for example, through magneto-elastic interaction. The presence of these quartic terms manifests through the appearance of charge peaks at twice the magnetic propagation vector [51]. Setting $\rho = s_z/s_x$, the two expressions to minimize in the presence of umklapp become:

$$E = \frac{s_x^2}{2}\left[(J_1 + J_2)(1 - \rho^2) + J'(1 + \rho^2) + 2\Gamma\rho^2 + \cos\alpha\left[(J_1 + J_2)(1 + \rho^2) + J'(1 - \rho^2) - 2\Gamma\rho^2\right]\right] \quad \text{for } \beta = 0 \tag{12}$$

and

$$E = \frac{s_x^2}{2}\left[(-J_1 + J_2)(1 - \rho^2) - J'(1 + \rho^2) + 2\Gamma\rho^2 + \cos\alpha\left[(-J_1 + J_2)(1 + \rho^2) - J'(1 - \rho^2) - 2\Gamma\rho^2\right]\right] \quad \text{for } \beta = \pi. \tag{13}$$

With the help of equations (9), (11), (12) and (13) one can construct phase diagrams for what is effectively a two-parameter problem. The case relevant for RMn_2O_5 is that of $J_2 < 0$, since, as we mentioned previously, the interaction through the Mn^{3+} layer is always ferromagnetic. Figure 9 shows the phase diagram at fixed $J_2 = -1$ as a function of J_1 and J' and in the isotropic case ($s_x = \pm s_z$, $\Gamma = 0$). We have plotted only the region in which J_2 is the largest exchange constant—a plausible assumption, as we have seen, but the extended phase diagram is equally easy to plot.

The following observations can be made by inspecting the phase diagrams:

(i) Even in the absence of umklapp, there are two large regions of commensurability. For $\beta = 0$ the magnetic cell coincides with the chemical cell, whereas for $\beta = \pi$ the magnetic cell is doubled.

(ii) More significantly, $\alpha = 0$ *always* whenever $\beta = 0$ or π. This is also clear by inspecting equations (12) and (13), since this expression is minimized for one of the extrema of $\cos\alpha$. Since $\alpha = 0$ in this part of the phase diagram, the solution is a collinear AFM, and the terms containing ρ and Γ in equations (12) and (13) cancel out. This is very important, since it indicates that this simple model is incapable of reproducing the $BiMn_2O_5$ situation, where the presence of a s_z component indicates that $\alpha > 0$ even with $\beta = \pi$ (propagation vector $\mathbf{q} = (\frac{1}{2}, 0, \frac{1}{2})$).

(iii) As soon as one departs from the isotropic situation, the umklapp terms tend to stabilize the commensurate phases, and the region of incommensurability shrinks. For $\rho = 0.5$, the portion of the phase diagram shown in figure 9 is completely commensurate with $\alpha = 0$, and is split diagonally (top left to bottom right) between $\beta = 0$ (bottom) and $\beta = \pi$ (top). Typical experimental values of ρ are even smaller—of the order of 0.2.

(iv) Even in the presence of umklapp, one can always find small patches of incommensurability in the extended phase diagram. However, in order to stabilize the RMn_2O_5 incommensurate phase by this mechanism, one would require extremely fine-tuning of the exchange parameters.

One also observes that there is complete degeneracy between the configurations differing by the sign of the z components of the spins ($\alpha \to -\alpha$, $\beta \to -\beta$), corresponding to the counter-clockwise and clockwise rotation of the cycloids (if one imagines traveling along the positive z direction), and to the two different polarities of the magnetic structure (there is no true chirality here). This is completely trivial in this simple 1D model, but not so in the realistic situation of RMn_2O_5, since, as we have seen, the in-plane magnetic structure also has a polarity, and reversing all the z components would correspond to a non-symmetry equivalent domain (see section 10 below). The degeneracy between these domains must be lifted to some degree, in order to enable the observation of a s_z component by diffraction.

This observation, together with those at points (ii) and (iv) above, suggest that an additional mechanism, in addition to competition between NN and NNN interactions, may be required to explain the observed phase diagram of RMn_2O_5.

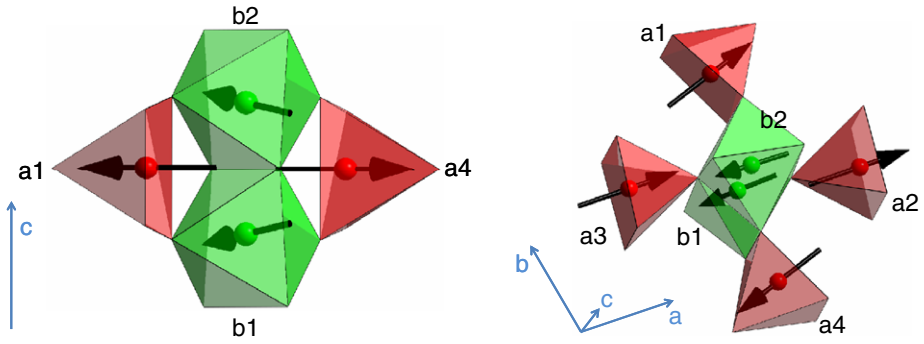

Figure 8. Magnetic site labeling scheme employed for the calculation of the DM energy (from [19]).

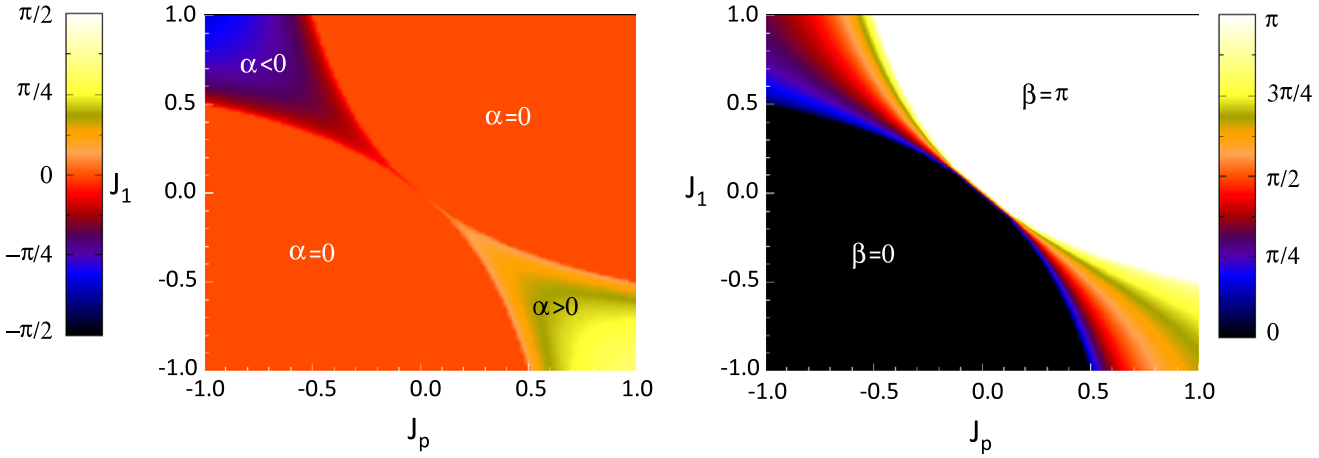

Figure 9. Phase diagram for the $J_1 - J_2 - J'$ model for $J_2 = -1$ and $\Gamma = 0$ (isotropic case). Areas in solid colors indicate commensurate phases, whereas a color gradation indicates incommensurability. The angle α is twice the phase offset between sites S_1 and S_2, whereas β is the propagation vector q_z times 2π (see text).

9. Dzyaloshinskii–Moriya interaction and its consequences for the RMn_2O_5 magnetic structures

As we have seen, the simple model presented in section 8 is incapable of reproducing some important features found in RMn_2O_5 compounds—for example the presence of a small s_z component in $BiMn_2O_5$. Moreover, opposite cycloidal polarities (i.e. opposite signs of s_z, everything else being equal) are energetically degenerate, while this degeneracy must be lifted to be consistent with the diffraction observations. In fact, this degeneracy is characteristic of all models that contain symmetric exchange terms only, at least for phases that retain part of the crystallographic symmetry. In fact, symmetric coupling energy terms that split the degeneracy must be of the form $S_x^i S_z^j$ or $S_y^i S_z^j$, where i and j refer to different magnetic sites. If a set of mirror planes perpendicular to the c-axis is retained, as is the case, for example, for the commensurate phase of RMn_2O_5 [19], terms of this form cancel out exactly by symmetry. It is therefore useful to look specifically for an antisymmetric interaction term that is capable of lifting the degeneracy.

In the crystal structure of the paramagnetic phases, the DM vector **D** between Mn^{4+} atoms chained along the z-axis is identically zero, because these sites are related by inversion (figure 8). In the ferroelectric phase, this is no longer strictly true, because the ferroelectric displacements break inversion symmetry. However, these displacements are extremely small, and so should also be the resulting **D** vector. Here we show that there is a much more efficient mechanism for generating non-collinearity along the z-axis, through an effective antisymmetric interaction mediated by the Mn^{3+} atoms. Mn^{3+} and Mn^{4+} atoms are not related by any symmetry, and the **D** vector associated with pairs of such atoms is in no way restricted. However, **D** transforms like an axial vector between symmetry-related bonds, so some of the DM interaction terms cancel out by symmetry. The labeling scheme we employ to calculate the DM energy is shown in figure 8, and is consistent with [19]:

$$\begin{aligned}
\mathbf{D}^{\parallel}_{1-4} &= -\mathbf{D}^{\parallel}_{2-4} = -\mathbf{D}^{\parallel}_{1-1} = \mathbf{D}^{\parallel}_{2-1} \\
\mathbf{D}^{\perp}_{1-4} &= \mathbf{D}^{\perp}_{2-4} = \mathbf{D}^{\perp}_{1-1} = \mathbf{D}^{\perp}_{2-1} \\
\mathbf{D}^{\parallel}_{1-2} &= -\mathbf{D}^{\parallel}_{2-2} = -\mathbf{D}^{\parallel}_{1-3} = \mathbf{D}^{\parallel}_{2-3} \\
\mathbf{D}^{\perp}_{1-2} &= \mathbf{D}^{\perp}_{2-2} = \mathbf{D}^{\perp}_{1-3} = \mathbf{D}^{\perp}_{2-3}
\end{aligned} \tag{14}$$

where $\mathbf{D}^{\parallel}$ and $\mathbf{D}^{\perp}$ are the components of the DM vector parallel/perpendicular to the ab plane. By employing

equation (14) we can calculate the DM energy $E_{\rm DM}$:

$$\begin{aligned} E_{\rm DM} &= \mathbf{D}^{\parallel}_{1-4}\cdot[(\mathbf{S}_{a4}-\mathbf{S}_{a1})\times(\mathbf{S}_{b1}-\mathbf{S}_{b2})] \\ &\quad + \mathbf{D}^{\perp}_{1-4}\cdot[(\mathbf{S}_{a4}+\mathbf{S}_{a1})\times(\mathbf{S}_{b1}+\mathbf{S}_{b2})] \\ &\quad + \mathbf{D}^{\parallel}_{1-2}\cdot[(\mathbf{S}_{a2}-\mathbf{S}_{a3})\times(\mathbf{S}_{b1}-\mathbf{S}_{b2})] \\ &\quad + \mathbf{D}^{\perp}_{1-2}\cdot[(\mathbf{S}_{a2}+\mathbf{S}_{a3})\times(\mathbf{S}_{b1}+\mathbf{S}_{b2})] \\ &= \simeq 2\mathbf{D}^{\parallel}_{1-4}\cdot[\mathbf{S}_{a4}\times(\mathbf{S}_{b1}-\mathbf{S}_{b2})]+2\mathbf{D}^{\perp}_{1-2}\cdot[\mathbf{S}_{a2}\times(\mathbf{S}_{b1}+\mathbf{S}_{b2})]\,. \end{aligned} \tag{15}$$

In the last line of equation (15) we have exploited the fact that $\mathbf{S}_{a4} \simeq -\mathbf{S}_{a1}$ and $\mathbf{S}_{a2} \simeq \mathbf{S}_{a3}$ (the equality is exact for fully constrained models and $q_x = 1/2$). One should also remark that for the commensurate phases $\mathbf{S}_{a2}$ is essentially in-plane—it is in fact exactly so by symmetry for $BiMn_2O_5$ and approximately for most of the other elements with $\mathbf{q} = (\frac{1}{2}, 0, \frac{1}{4})$. Therefore, the effect of the first term is clearly that of inducing a z component of opposite sign, and therefore a canting angle between $\mathbf{S}_{b1}$ and $\mathbf{S}_{b2}$. It is an effective antisymmetric interaction along the chain, mediated by the in-plane spins. The second term induces an in-plane canting angle between spins $\mathbf{S}_a$ and $\mathbf{S}_b$. Since this does not break the symmetry, we will not consider it in the remainder.

We can reproduce the effect of the first term in our simple one-dimensional model by making a correspondence between spins in figures 7 and 8 and setting the DM vector along the b-axis, i.e. $\mathbf{D}^{\parallel}_{1-4} = \hat{\mathbf{j}}D$. We also assume $\mathbf{S}_{a4} = \tilde{s}_x \cos\beta R_z$. After some manipulations we obtain:

$$\begin{aligned} E_{\rm DM} &= \frac{2D}{N}\sum_{R_z}\tilde{s}_x s_z \cos\beta R_z \\ &\quad \times \left[\sin(\beta R_z - \alpha/2) - \sin(\beta R_z + \alpha/2)\right] \\ &= -D\tilde{s}_x s_z \sin\alpha/2. \end{aligned} \tag{16}$$

It is clear that $E_{\rm DM}$ stabilizes a non-zero value of α even for the umklapp cases (equations (12) and (13)). This simple mechanism is therefore capable of explaining the observation of a small s_z component in the case of $BiMn_2O_5$, where $\beta = \pi$. We can see now that $E_{\rm DM}$ discriminates between right-handed and left-handed cycloids, since its sign is reversed if one changes the sign of α. In addition, the sign of α (reversal of cycloidal polarity) must change in response to a change in the sign of $\tilde{s}_x$. For a given s_x, changing the sign of $\tilde{s}_x$ corresponds to reversing the in-plane polarity of the spin system. Therefore, the DM term favors a consistent alignment of in-plane and cycloidal polarities, always parallel or always antiparallel depending on the sign of D. This lifts the degeneracy between the two types of non-symmetry-equivalent domains—an essential ingredient to explain why cycloids are observed at all by diffraction.

The effect of $E_{\rm DM}$ on the wider phase diagram, away from the umklapp points, is more difficult to calculate analytically. Preliminary numerical calculations suggest that, in addition to making α non-zero for the umklapp phases, the DM term has the additional effect of extending the region of incommensurability—unsurprisingly perhaps, because it promotes non-collinearity.

10. Magnetic domain switching under an applied electric field, spherical neutron polarimetry

The simple model outlined in sections 8 and 9 paints a picture of the RMn_2O_5 physics that is rather different from that of the typical cycloidal multiferroics. The case of $BiMn_2O_5$ demonstrates with particular clarity that the cycloidal component does not emerge independently as for $TbMnO_3$, but is induced by and has consistent polarity with the in-plane magnetic structure. The presence of an antisymmetric energy term that lifts the degeneracy between configurations with parallel and antiparallel polarities is also important, because it has a direct implication for the domain formation and the domain switching upon application of an electric field. In the presence of this term, if the configuration (α, β) is the stable state, the 'alternate' configuration with reversed cycloids, $(-\alpha, -\beta)$, is not an extremum of the energy function. However, if $E_{\rm DM}$ is small, in general there will be a local minimum near the $(-\alpha, -\beta)$ point, which corresponds to a metastable state. In this case, it is possible in principle to reverse one of the two polarities (in-plane or cycloidal) without affecting the other. Which of the two polarities is reversed depends on the specific coupling mechanism to the electric field; in other words, if the cycloids were entirely responsible for the electrical polarization through spin–orbit coupling, the direction of rotation of the cycloids must be reversed when the electrical polarization is reversed. Likewise, reversal of the in-plane polarity is a strict requirement of the exchange-striction model. For certain values of the parameter, the metastable minimum is very shallow or absent: in this case, we would expect that the electric field would switch the structure between truly degenerate domains related by inversion. We can summarize the different scenarios as follows (metastable states can be 'shallow' or 'deep' with respect to $k_{\rm B}T$):

(i) *FE by spin–orbit coupling, deep metastable state*. The prediction for this scenario is that only the cycloids will switch upon reversal of the electric polarization by an applied external field. The in-plane structure should remain unaffected.

(ii) *Both spin–orbit and exchange-striction contribute to FE, deep metastable state*. Here, both in-plane and cycloidal components should switch, possibly at different fields. This scenario is unlikely, as it should produce a two-step FE hysteresis loop that is not observed experimentally.

(iii) *FE by exchange-striction, deep metastable state*. Here, only the in-plane structure should switch, whereas the cycloids should not be affected.

(iv) *Any mechanism, shallow metastable states*. Here, the two components always switch simultaneously, so only domains related by inversion symmetry are ever observed.

A direct observation of the response of the magnetic structure to the reversal of an external electric field is therefore non-trivial and potentially informative about the mechanism of ferroelectricity.

Very few techniques are available to directly probe the domain structure of an antiferromagnet. Second-harmonic light generation (SHG) has been used successfully to this

effect in multiferroics—see for example [52]. However, this technique can only be used for 'Γ-point' antiferromagnets, in which the magnetic unit cell coincides with the primitive chemical cell. In fact, the macroscopic quantity that is relevant for magnetic SHG is a third-rank, time-reversal odd axial tensor. For non-Γ-point antiferromagnets, time-reversed translations are symmetry operators. Therefore, the magnetic point group contains time reversal, and the tensor is identically zero. Another way of saying the same thing is to observe that SHG is an optical technique, and should therefore only be sensitive to zone-center (Γ-point) effects. In these more complex cases, the technique of choice to probe antiferromagnetic domains is scattering of polarized neutrons, of which spherical neutron polarimetry (SNP) is a particularly powerful version. The neutron spin polarization is defined as the statistical average over the neutron beam of the expectation value of the quantum mechanical spin projection operator. An almost fully polarized (>99%) monochromatic neutron beam is generated by means of a Heusler crystal monochromator. The neutron spin direction can be altered in one of three ways:

(i) *adiabatic rotation*: the spins will follow a slowly varying magnetic field;
(ii) *precession*: when crossing an abrupt step change in the field direction, the neutron spins will precess around the new magnetic field;
(iii) *flip*: the neutron spins can be flipped by 180° by a special device, known as a flipper, which also exploits neutron spin precession.

By an appropriate combination of adiabatic rotations, precessions and flips, one can prepare the incident neutron polarization in an arbitrary direction, and also rotate the scattered polarization so that any of its components is parallel (or antiparallel) to the analysis direction. To this end, a flipper and a polarization analyzer, in this case a ^{3}He spin-filter, are placed in the scattered beam in front of the neutron detector. The sample itself is held in exactly zero magnetic field. Unlike conventional neutron crystallography, spherical polarimetry does not rely on measured neutron intensities, but on intensity ratios between parallel and antiparallel settings of the final flipper/analyzer pair. In practice, one can measure nine independent 'flipping ratios', by setting the incident and scattered polarization along the X, Y and Z directions (in appropriate coordinates, see [53]). All the elements of the resulting polarization matrix (for a complete treatment see [53, 54]) are sensitive to the magnetic structure factor, as is the unpolarized neutron scattering cross section. However, some of the matrix elements—in our case the elements P_{zx} and P_{yx}—carry unique information about the domain population, even if these domains are related by inversion.

We performed a SPN experiment on a YMn_2O_5 single crystal as a function of temperature and external electric field applied along the b crystallographic direction. The results of this experiment are described in detail in [20]. With the NPS technique, we can probe directly both domain structure and domain population for different temperatures and orientations of the external electric field. However, on D3, there is only limited access to reflections out of the horizontal scattering plane, so the crystal mounting will dictate which region of reciprocal space is observed. For this first experiment, we chose to mount the crystal with the b-axis vertical, i.e. perpendicular to the scattering plane, so that only reflections with $k = 0$ were accessible. This setting enabled us to probe in great detail the magnetic structure within the a–b plane, and to observe the effect of the domain switching on the in-plane structure. We were, however, not able to distinguish between stable and 'alternate' domains. Consequently, our experiment can completely corroborate or falsify scenario (i) above. It can also provide partial information about (ii), but it is unable to distinguish conclusively between (iii) and (iv). The main results of our experiment are summarized in figure 10. We applied two types of electric field-switching protocols: cooling in an applied electric field of either polarity (± 2.2 kV cm^{-1}) through the Nèel temperature T_N down to 25 K (left panel) and cycling the electric field at 35 K, i.e. closer to T_N, after polarizing the sample at 25 K. For in-field cooling, we observed a complete reversal of the in-plane domain population (figure 10, left). This clearly demonstrates that the in-plane magnetic structure is coupled to the electric field, ruling out scenario (i) above. At 35 K, we were able to measure a complete hysteresis loop on the off-diagonal neutron polarization matrix elements (figure 10, right). The loop is shifted downwards with respect to the centerline, indicating that some domains are 'locked' in a fixed polarization direction and cannot be reversed by the small electric field available to us. More importantly, the SNP results are in excellent agreement with measurements of the macroscopic electrical polarization performed with the same protocol, including the downward shift of the hysteresis loop and limiting values of the electrical polarization at the top and bottom of the hysteresis loop. In other words, the in-plane antiferromagnetic domain population is strictly proportional to the electrical polarization. This result indicates that, if both in-plane and cycloids contributed independently to the polarization (scenario (ii)), the latter contribution is probably very small. In a future experiment we are planning to perform an independent measurement of the cycloidal domain switching under similar conditions, by mounting the crystal with a different orientation. This will enable us to discriminate between the above scenarios in a unique way.

11. Outlook and conclusions

As we have seen in the previous sections, much progress has been made towards understanding the connections between magnetism and ferroelectricity in RMn_2O_5, thanks to the sustained efforts of several groups. Neutron diffraction played a major part in this research, providing several key pieces of information. Nonetheless, much remains to be done. The most obvious gap is the lack of a definitive determination of the magnetic structures of the two ICPs. The HT-ICP is clearly the most difficult one, because the magnetic moments are small, and no solution has been proposed to date. Starting form the 1970s, several groups have attempted to solve the magnetic structure of the LT-ICP, from both powder [42, 38] and single-crystal data [39, 43, 48]. Some features are common to all these

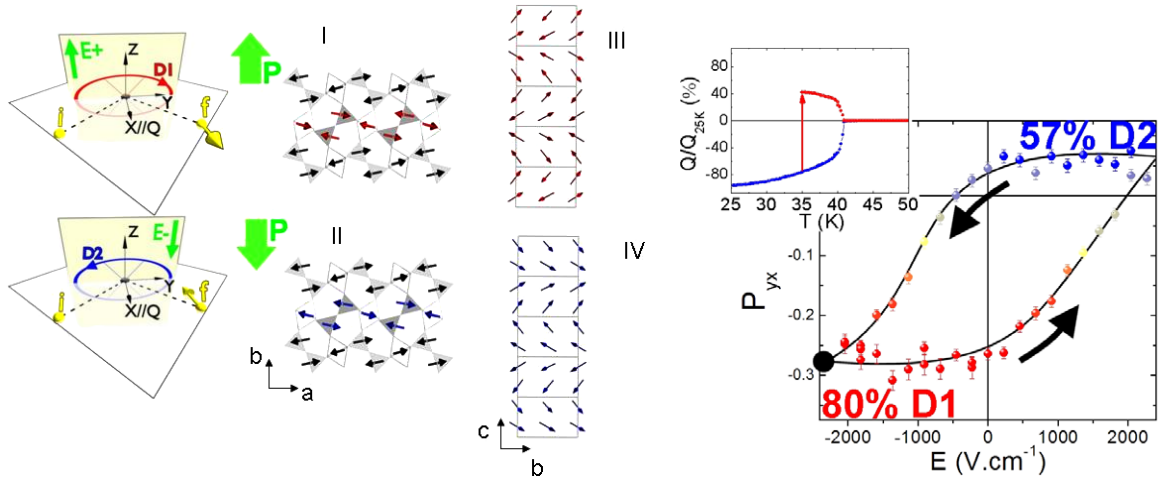

Figure 10. Left: schematic representation of the neutron spherical polarimetry experiment for the two domains, here shown in the idealized case of an unpolarized incident beam. The real (or imaginary) component of the magnetic structure factor projection $M^{\perp}_{hkl}$ rotate clockwise (counter clockwise) for domain I (domain II), creating a spin polarization of opposite signs for the scattered neutron. The direction of the applied electric field is also indicated. Right: magnetic structures of YMn_2O_5 for the different domain configurations, projected on the *ab* plane (I and II) and the *bc* plane (III and IV). Small arrows represent magnetic moments. The observed domain switching mechanism is represented by the inversion (change from the red to the blue) in the central chain (between configurations I and II in the *ab* plane). Right panel: partial hysteresis loop measured on the created neutron polarization element P_{yx} for the $-\frac{1}{2}\ 0\ -\frac{7}{4}$ Bragg peak of an YMn_2O_5 crystal, warmed to 35 K after previous cooling to 25 K under a negative -2.2 kV cm^{-1} electric field. Inset: integrated pyroelectric currents measured on a 0.5 mm thick YMn_2O_5 crystal of the same batch on cooling to 25 K in a negative -2.0 kV cm^{-1} electric field (bottom/blue curve), followed by warming to 35 K and switching to a positive $+2.0$ kV cm^{-1} electric field (top/red curve). The data are normalized to the fully saturated value at 25 K. Both hysteresis bias and the switching ratios are in very good agreement with the neutron data.

refinements, and can be considered as established with good confidence. Other aspects are slowly emerging as techniques and refinements improve. The main results to date can be summarized as follows:

(i) In the LT-ICP, the modulations of the two zig-zag chains are approximately *in quadrature*, rather than *in-phase*, as in the CP. This emerges clearly from both the powder data [38] and the more recent single-crystal data [48]. This is a key feature in the context of the exchange-striction model, since it explains why ferroelectricity is suppressed in the LT-ICP: in fact, all terms in exchange-striction polar vector E_y (equation (2)) contain the cosines of the phase differences between atoms on different zig-zag chains. If the phase difference between these chains is close to 90°, the cosines will be small and so will be the electrical polarization.

(ii) In the LT-ICP magnetic structure, one can recognize 'patches' resembling CP domains [38]. Both polarities are equally represented, so their contributions to ferroelectricity cancel out. These 'patches' alternate with regions where the dot product between sites on the two chains is very small or zero, yielding a negligible contribution to ferroelectricity.

(iii) The main difference between the powder structure [38] and the more recent (and accurate) single-crystal structure [48] is the relative phase of the *b* component of the spins. In the latter, the S_x and S_y components are *in quadrature* yielding a cycloidal component in the *a*–*b* plane. Here, the spins of the two chains are almost orthogonal throughout the modulated structure. This has no impact on the exchange-striction polar vector calculation, since the two components contribute independently to E_y, but may provide an additional spin–orbit contribution. We remark that if the two zig-zag chain modulations were identical except for a phase factor—a reasonable hypothesis—this new spin–orbit contribution would be directed entirely along the *b*-axis.

(iv) Assessing the spin–orbit polar vector in the LT-ICP requires a level of accuracy in the magnetic structure determination that, in our opinion, has not yet been attained. In section 7, we present the results based on the recent determination by Kim *et al* [48], which are not in accord with the experimental values of the electrical polarization. We remark, however, that the structure by Kim *et al* is not yet completely satisfactory, since symmetry-equivalent atoms have widely different modulation amplitudes. We believe that these inconsistencies should be resolved before a final assessment of the relative importance of the two mechanisms can be made.

Another aspect that so far remains largely unexplored is that of rare-earth magnetic ordering. It is now known that a sizeable magnetic moment is induced on the rare-earth by the ordering of Mn (see, for example, [51]). Some aspect of the low-temperature ordering and the effect of the application of an external magnetic field have also been established [32]. However, the dramatic changes of the electrical polarization upon rare-earth magnetic ordering have not been explained. The study of rare-earths with different on-site anisotropy may provide important clues for understanding these effects.

In summary, we have presented an overview of the neutron diffraction results for the RMn_2O_5 multiferroics, with particular emphasis on the correlations between magnetic ordering and ferroelectricity. Solely on the basis of the refined magnetic structures, we calculate polar vector quantities that can be directly related to the electrical polarization, for both exchange-striction and spin–orbit microscopic models of the dominant magneto-electric interactions. We also explored the underlying causes giving rise to the complex magnetic phase diagram of RMn_2O_5, and proposed a 'minimal' model that can reproduce some of the observed features whilst highlighting the importance of antisymmetric exchange in stabilizing phases of consistent polarity. Finally, we illustrated what in our opinion are the missing 'pieces of the puzzle' required to understand fully the phenomenology of these remarkable materials.

References

[1] Catalan G and Scott J F 2007 *Nature* **448** E4–5
[2] Eerenstein W, Mathur N D and Scott J F 2006 *Nature* **442** 759–65
[3] Hur N, Park S, Sharma P, Ahn J, Guha S and Cheong S 2004 *Nature* **429** 392–5
[4] Kimura T, Goto T, Shintani H, Ishizaka K, Arima T and Tokura Y 2003 *Nature* **426** 55–8
[5] Mostovoy M 2008 *Nat. Mater.* **7** 269–70
[6] Cheong S W and Mostovoy M 2007 *Nat. Mater.* **6** 13–20
[7] Radaelli P G and Chapon L C 2007 *Phys. Rev.* B **76** 054428
[8] Harris A B 2007 *Phys. Rev.* B **76** 054447
[9] Harris A 2006 *J. Appl. Phys.* **99** 08E303
[10] Mostovoy M 2006 *Phys. Rev. Lett.* **96** 067601
[11] Kenzelmann M, Harris A, Jonas S, Broholm C, Schefer J, Kim S, Zhang C, Cheong S, Vajk O and Lynn J 2005 *Phys. Rev. Lett.* **95** 087206
[12] Kimura T, Lawes G, Goto T, Tokura Y and Ramirez A 2005 *Phys. Rev.* B **71** 224425
[13] Jia C, Onoda S, Nagaosa N and Han J H 2007 *Phys. Rev.* B **76** 144424
[14] Lawes G, Kenzelmann M, Rogado N, Kim K, Jorge G, Cava R, Aharony A, Entin-Wohlman O, Harris A, Yildirim T, Huang Q, Park S, Broholm C and Ramirez A 2004 *Phys. Rev. Lett.* **93** 247201
[15] Rogado N, Lawes G, Huse D, Ramirez A and Cava R 2002 *Solid State Commun.* **124** 229–33
[16] Nagaosa N 2008 *J. Phys. Soc. Japan* **77** 031010
[17] Higashiyama D, Miyasaka S and Tokura Y 2005 *Phys. Rev.* B **72** 064421
[18] Kimura H, Kobayashi S, Fukuda Y, Osawa T, Kamada Y, Noda Y, Kagomiya I and Kohn K 2007 *J. Phys. Soc. Japan* **76** 074706
[19] Vecchini C, Chapon L, Brown P, Chatterji T, Park S, Cheong S W and Radaelli P 2008 *Phys. Rev.* B **77** 134434
[20] Radaelli P, Chapon L, Daoud-Aladine A, Vecchini C, Brown P, Chatterji T, Park S and Cheong S W 2008 *Phys. Rev. Lett.* at press (*Preprint* 0803.3736)
[21] Rodriguez-Carvajal J 1993 *Physica* B **192** 55–69
[22] Blake G, Chapon L, Radaelli P, Park S, Hur N, Cheong S and Rodriguez-Carvajal J 2005 *Phys. Rev.* B **71** 214402
[23] Alonso J, Casais M, MartinezLope M, Martinez J and FernandezDiaz M 1997 *J. Phys.: Condens. Matter* **9** 8515–26
[24] Kagomiya I, Kohn K and Uchiyama T 2002 *Ferroelectrics* **280** 297–309
[25] Kobayashi S, Kimura H, Noda Y and Kohn K 2005 *J. Phys. Soc. Japan* **74** 468–72
[26] Munoz A, Alonso J, Casais M, Martinez-Lope M, Martinez J and Fernandez-Diaz M 2002 *Phys. Rev.* B **65** 144423
[27] Munoz A, Alonso J, Casais M, Mairtinez-Lope M, Martinez J and Fernandez-Diaz M 2005 *Eur. J. Inorg. Chem.* 685–91
[28] Kobayashi S, Osawa T, Kimura H, Noda Y, Kagomiya I and Kohn K 2004 *J. Phys. Soc. Japan* **73** 1031–5
[29] Kobayashi S, Osawa T, Kimura H, Noda Y, Kagomiya I and Kohn K 2004 *J. Phys. Soc. Japan* **73** 1593–6
[30] Kobayashi S, Osawa T, Kimura H, Noda Y, Kasahara N, Mitsuda S and Kohn K 2004 *J. Phys. Soc. Japan* **73** 3439–43
[31] Kobayashi S, Osawa T, Kimura I, Noda Y, Kagomiya I and Kohn K 2005 *J. Korean Phys. Soc.* **46** 289–91
[32] Chapon L, Blake G, Gutmann M, Park S, Hur N, Radaelli P and Cheong S 2004 *Phys. Rev. Lett.* **93** 177402
[33] Ewings R A, Boothroyd A T, McMorrow D F, Mannix D, Walker H C and Wanklyn B 2008 *Phys. Rev.* B **77** 104415
[34] Ratcliff W, Kiryukhin V, Kenzelmann M, Lee S, Erwin R, Schefer J, Hur N, Park S and Cheong S 2005 *Phys. Rev.* B **72** 060407
[35] Kang S H, Lee H J, Kim I W, Jang T H, Jeong Y H and Koo T Y 2007 *J. Korean Phys. Soc.* **51** 669–73
[36] Hur N, Park S, Sharma P, Guha S and Cheong S 2004 *Phys. Rev. Lett.* **93** 107207
[37] Fukunaga M, Nishihata K, Kimura H, Noda Y and Kohn K 2007 *J. Phys. Soc. Japan* **76** 074710
[38] Chapon L, Radaelli P, Blake G, Park S and Cheong S 2006 *Phys. Rev. Lett.* **96** 097601
[39] Wilkinson C, Sinclair F, Gardner P, Forsyth J and Wanklyn B 1981 *J. Phys. C: Solid State Phys.* **14** 1671–83
[40] Kimura H, Kamada Y, Noda Y, Kaneko K, Metokii N and Kohn K 2006 *J. Phys. Soc. Japan* **75** 113701
[41] Buisson G 1973 *Phys. Status Solidi* a **17** 191–8
[42] Buisson G 1973 *Phys. Status Solidi* a **16** 533–43
[43] Gardner P, Wilkinson C, Forsyth J and Wanklyn B 1988 *J. Phys. C: Solid State Phys.* **21** 5653–61
[44] Rodriguez-Carvajal J, Hennion M, Moussa F and Moudden A 1998 *Phys. Rev.* B **57** R3189–92
[45] Wang C, Guo G C and He L 2007 *Phys. Rev. Lett.* **99** 177202
[46] Wang C, Guo G C and He L 2008 *Phys. Rev.* B **77** 134113
[47] Vecchini C, Radaelli P and Chapon L 2008 *Phys. Rev.* B **77** 134434
[48] Kim J H, Lee S H, Park S, Kenzelmann M, Schefer J, Chung J H, Majkrzak C, Takeda M, Wakimoto S, Park S Y, Cheong S W, Matsuda M, Kimura H, Noda Y and Kakurai K 2008 *Preprint* 0803.1123
[49] Harris A B, Kenzelmann M, Aharony A and Entin-Wohlman O 2008 *Preprint* 0803.0945
[50] Harris A B, Aharony A and Entin-Wohlman O 2008 *Preprint* 0802.0604
[51] Beutier G, Bombardi A, Vecchini C, Radaelli P G, Park S, Cheong S W and Chapon L C 2008 *Phys. Rev.* B **77** 172408
[52] Fiebig M, Lottermoser T, Frohlich D, Goitsev A and Pisarev R 2002 *Nature* **419** 818–20
[53] Blume M 1963 *Phys. Rev.* **1** 1670
[54] Maleev S, Baryakhtar V and Suris R 1963 *Sov. Phys.—Solid State* **4** 2533–9